

# First-Principles Simulations of Tip Enhanced Raman Scattering Reveal Active Role of Substrate on High-Resolution Images

Y. Litman,<sup>\*,†,‡,¶</sup> F. P. Bonafé,<sup>‡,¶</sup> A. Akkoush,<sup>‡,§</sup> H. Appel,<sup>‡</sup> and M. Rossi<sup>\*,‡,§</sup>

<sup>†</sup>*Yusuf Hamied Department of Chemistry, University of Cambridge, Lensfield Road, Cambridge, CB2 1EW, United Kingdom*

<sup>‡</sup>*MPI for the Structure and Dynamics of Matter, Luruper Chaussee 149, 22761 Hamburg, Germany*

*¶These authors contributed equally*

<sup>§</sup>*Fritz Haber Institute of the Max Planck Society, Faradayweg 4–6, 14195 Berlin, Germany*

E-mail: yl899@cam.ac.uk; mariana.rossi@mpsd.mpg.de

## Abstract

Tip-enhanced Raman scattering (TERS) has emerged as a powerful tool to obtain sub-nanometer spatial resolution fingerprints of atomic motion. Theoretical calculations that can simulate the Raman scattering process and provide an unambiguous interpretation of TERS images often rely on crude approximations of the local electric field. In this work, we present a novel and first principles based method to compute TERS images by combining Time Dependent Density Functional Theory (TD-DFT) and Density Functional Perturbation Theory (DFPT) to calculate Raman cross sections with realistic local fields. We present TERS results on the benzene and TCNE molecule, the latter of which is adsorbed at Ag(110). We demonstrate that chemical effects on chemisorbed molecules, often ignored in TERS simulations of

medium and large systems sizes, dramatically change TERS images. This calls for the inclusion of chemical effects for predictive theory-experiment comparisons and understanding of molecular motion at the nanoscale.

Atomic motion in materials and molecules drives their structural changes and chemical reactions, thus are fundamental importance in areas as diverse as efficient device fabrication and biochemistry. Usually, vibrational modes are characterized indirectly through vibrational spectroscopy techniques that are incapable of resolving the motion of individual nuclei.

Visualizing such motions with high spatial and temporal resolution is a long-sought goal that would allow an unambiguous understanding of certain physical and chemical processes.<sup>1</sup> For individual molecules adsorbed on certain substrates, this goal has been recently addressed by tip-enhanced Raman scattering (TERS).<sup>2</sup>

TERS spectroscopy is a powerful technique developed in the last two decades that seamlessly integrates the chemical specificity provided by Raman spectroscopy with the spatial sensitivity of scanning probe microscopy (SPM).<sup>3-6</sup> Similar to other surface-enhanced techniques, the working principle of TERS relies on using the strongly localized plasmonic field produced at the tip apex by an external electromagnetic field, which enhances the Raman signal by several orders of magnitude.<sup>7,8</sup> Unlike conventional spectroscopic techniques, where the spatial resolution is limited by the Rayleigh diffraction limit, near-field enhanced techniques do not present this optical restriction. Indeed, depending on the shape of the tip apex and other experimental parameters, TERS setups can lead to subnanometer spatial resolution.<sup>9</sup> TERS has been used to monitor catalytic processes at the nanoscale,<sup>10</sup> study plasmon-driven chemical reactions,<sup>11</sup> characterization of 2D materials,<sup>12-14</sup> and to probe redox reactions at the solid/liquid interface.<sup>15,16</sup> Arguably, the most impressive achievement obtained with TERS is the real space visualization of the vibrational modes of a single molecule, reported a few years ago.<sup>2</sup>

Regarding the physical processes underlying single-molecule TERS and the associated simulation protocols, there are still many points that need clarification. Besides the enhancement due to the strong localization of plasmonic electromagnetic fields (EM), there are three other possible

enhancement mechanisms normally discussed in the literature and referred to as “chemical mechanisms”:<sup>17</sup> i) The enhancement due to the chemical interaction (e.g. orbital hybridization) between molecule and substrate or molecule and tip in the electronic ground state (chem-GS); ii) The enhancement due to a resonance of the external field with a molecular electronic transition (chem-R); iii) The enhancement due to a charge transfer caused by the excitation-induced charge reorganization between the molecule and substrate or tip (chem-CT). While the EM mechanism is believed to be dominant in most cases, its relative importance is still under debate<sup>18–20</sup> For example, when the distance between a tip and a molecule is small enough to form a molecular point contact, a dramatic enhancement likely due to a chem-CT enhancement has been reported.<sup>21–24</sup>

Several methods to simulate TERS spectroscopy have been recently developed, with the aim of helping to interpret the increasing amount of experimental observations. There are methods based on phenomenological assumptions, which describe the localization of the near field by a bell-shaped function with a predefined width<sup>2,25,26</sup> or which describe the local field by an oscillating dipole.<sup>27,28</sup> These methods are relatively easy to implement and computationally inexpensive, but they are not *ab initio* and thus have limited predictive power. Other methods incorporate a realistic (classical) description of the near field,<sup>28–32</sup> but the computational cost becomes prohibitively expensive for medium-sized systems, and a quantum description is restricted to (small) gas-phase molecules. While all these methods have provided valuable insights in specific situations, it is known that the exact atomistic structure of the tip influences the near field in nanoplasmonic junctions,<sup>33–35</sup> and that considering the electronic quantum effects in the description of nanoplasmonic fields is mandatory in certain conditions.<sup>33,35</sup>

In this work, we present a methodology that bridges a gap between some of the existing approaches. Our methodology incorporates a realistic description of the near field and retains a modest computational cost, making it applicable to adsorbed and large molecules. To achieve this, we employ density functional perturbation theory (DFPT) to compute the electric-field response of the electronic density that defines the non-resonant vibrational Raman cross sections, but incorporate a realistic near-field distribution which we obtain from time-dependent density functional

theory (TDDFT) calculations of different atomistic tip geometries. In this way, we can capture the chem-GS and EM Raman enhancement mechanisms in our calculations, at a cost comparable to phenomenological methods for medium and large systems, but within a first-principles framework.

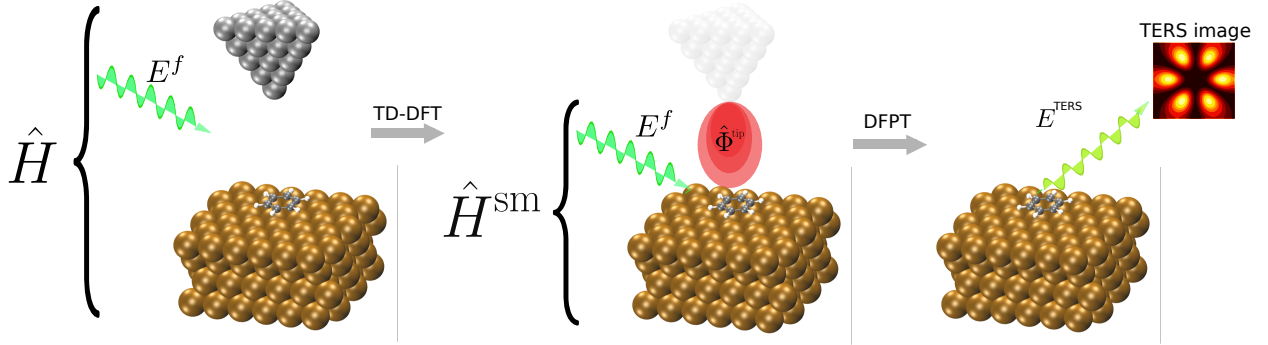


Figure 1: Schematic depiction of the proposed method. The full system and its corresponding full Hamiltonian,  $\hat{H}$  (left), are approximated by that of the substrate-molecule subsystem,  $\hat{H}^{\text{sm}}$  (center), which includes the perturbative terms associated with the external far field,  $E^f$ , and the local field generated by the tip plasmonic oscillations,  $\hat{\Phi}^{\text{tip}}$ , obtained from TDDFT calculations. The calculation of TERS spectra proceeds through density-functional perturbation theory for the calculation of polarizability tensors.

We consider a system composed of a molecule placed between a substrate and a metallic tip, that lies at some position above the molecule (see Fig. 1). If the distance between the tip and the substrate is larger than a few angstroms, there is no overlap of the corresponding charge densities, and therefore the interaction between the two components is dictated essentially by classical electrostatics.<sup>36</sup> We study the effect induced on this system by a time-dependent transverse electromagnetic field, hereafter referred to as the external far field. Within the dipole approximation, this field is homogeneous. By formally separating the tip Hamiltonian from that of the rest of the system, we can write

$$\hat{H}(t) = \hat{H}_0^{\text{sm}} - \hat{\boldsymbol{\mu}}^{\text{sm}} \cdot \mathbf{E}^f(t) + \hat{H}_0^{\text{tip}} - \hat{\boldsymbol{\mu}}^{\text{tip}} \cdot \mathbf{E}^f(t) + \hat{V}^{\text{int}}(t), \quad (1)$$

where the labels ‘sm’, ‘tip’ and ‘int’ refer to the substrate plus molecule subsystem, the tip subsystem, and the interaction between subsystems, respectively.  $H_0$  refers to the unperturbed Hamiltonians,  $\hat{\boldsymbol{\mu}}$  are the corresponding dipole operators, and  $\mathbf{E}^f(t) = (\lambda_x \hat{n}_x + \lambda_y \hat{n}_y + \lambda_z \hat{n}_z) \cos(\omega_0 t)$ ,

where  $\lambda_{x,y,z}$  are the electromagnetic field strengths,  $\omega_0$  the electromagnetic field frequency, and  $\hat{n}_{x,y,z}$  are unit vectors along each Cartesian direction. In the expression above, it is implicit that we work in the Coulomb gauge.

To move forward we make further assumptions. The first is that the tip is not influenced by the presence of the molecule and substrate (justified by the already-assumed far distance between these components and a neutral molecule-substrate subsystem). This allows the calculation of the time-dependent electronic density  $\rho_{\text{tip}}$  by the real-time propagation of the Kohn-Sham states of the isolated tip under the influence of an external field in TDDFT, assuming a dipolar light-matter coupling. Then, the (electrostatic) interaction between the tip and the rest of the system can be computed as

$$\hat{V}_{\text{int}}(\mathbf{r}_{\text{sm}}, t; \mathbf{R}_{\text{tip}}) = \int d\mathbf{r} \frac{\rho_{\text{tip}}(\mathbf{r}, t; \mathbf{R}_{\text{tip}})}{|\mathbf{r} - \hat{\mathbf{r}}_{\text{sm}}|} = \hat{\Phi}_{\text{tip}}(\mathbf{r}_{\text{sm}}, t; \mathbf{R}_{\text{tip}}), \quad (2)$$

where  $\mathbf{r}_{\text{sm}}$  refers to the positions of the electrons belonging to the substrate-molecule subsystem and  $\mathbf{R}_{\text{tip}}$  refers to the position of nuclei of the tip subsystem. In Eq. 2, we have defined the time-dependent electrostatic potential of the tip,  $\hat{\Phi}_{\text{tip}}$  (often called Hartree potential), which is a central quantity for the current method. Indeed, under the current assumptions, the effect exerted on the substrate by the tip can be described by its Hartree potential. The ‘;’ symbol in Eq. 2 has been used to emphasise the parametric dependence of  $\hat{\Phi}_{\text{tip}}$  on the position and spatial arrangement of the nuclei in the tip,  $\mathbf{R}_{\text{tip}}$ .

The second assumption is that the strength of the external far field is small, such that the response of the tip lies in the linear regime, i.e. one can perform a Taylor expansion of  $\hat{\Phi}_{\text{tip}}$  around zero-field strength ( $\lambda = 0$ ) and truncate it at first order. Then, considering that the system is at the ground state before an excitation by the laser field,  $\hat{\Phi}^{\text{tip}}(t = 0) = \hat{\Phi}_{\text{GS}}^{\text{tip}}$ , and that responses are local in the frequency domain in the linear regime,<sup>37</sup> we can write the substrate-molecule Hamiltonian

in a particular Cartesian direction  $\alpha$  as,

$$\hat{H}^{\text{sm}} = \hat{H}_0^{\text{sm}} + \hat{\Phi}_{\text{GS}}^{\text{tip}} + \lambda_\alpha \left[ -\hat{\mu}_\alpha^{\text{sm}} + \frac{\partial \tilde{\Phi}_{\text{tip}}(\omega_0; \mathbf{R}_{\text{tip}})}{\partial \lambda_\alpha} \Big|_{\lambda_\alpha=0} \right], \quad (3)$$

where  $\tilde{\Phi}_{\text{tip}}(\omega_0; \mathbf{R}_{\text{tip}})$  denotes a time Fourier transform of  $\hat{\Phi}_{\text{tip}}(t; \mathbf{R}_{\text{tip}})$  evaluated at  $\omega_0$ . In the last line, a perturbation of the substrate-molecule subsystem is neatly defined. The first term inside the square brackets describes the dipole interaction between the substrate with the homogeneous far field while the second term describes the interaction with the local field generated by the tip. The latter term gives rise to the EM enhancement mechanism and the modified selection rules present in TERS spectroscopy. See a more detailed derivation of Eq. 3 in Section I of the Supporting Information (SI). Eq. 3 is suitable to be treated within the *time-independent* DFPT in order to find the static polarizability of the molecule and substrate,  $\alpha$ , which enables the calculation of the non-resonant Raman signal.<sup>38</sup> In this work we calculate harmonic non-resonant Raman intensities,  $I^{\text{Raman}}_{\text{as}}$

$$I^{\text{Raman}}(\omega_i) \propto \left| \frac{\partial \alpha_{zz}}{\partial Q_i} \right|^2 \quad (4)$$

where  $\alpha_{zz}$  is the  $zz$  component of the polarizability tensor (a direction normally regarded as the most relevant in TERS experiments), and  $Q_i$  and  $\omega_i$  represent the eigenmode and eigenfrequency of the  $i$ -th vibrational normal mode, respectively. We stress that the method can also be applied to other approximations of the Raman signal, as e.g. from time correlation function approaches,<sup>39,40</sup> and allows for the evaluation of all Raman scattering directions.

In Fig. 1, we show a schematic depiction of the proposed method. The electronic oscillations created by the external field generate an oscillating Hartree potential,  $\hat{\Phi}^{\text{tip}}$ , whose gradient is the so-called local (longitudinal) electric field, and its maximum intensity is situated a few angstroms below the tip apex.<sup>41</sup> The advantage of centering the approach on  $\hat{\Phi}^{\text{tip}}$  rather than the local field and its gradient, is, besides its mathematical simplicity, the fact that all the terms in the multipolar

expansion are automatically incorporated and no origin-dependence problems arise. All magnetic contributions are ignored as usually done for non-magnetic materials.<sup>42</sup> Since the enhancement of the incident field is included but the enhancement of scattered field is ignored, we note that the predicted TERS intensity follows a  $|E|^2$  dependence instead of the expected  $|E|^4$  dependence<sup>17,43</sup>.

We start by analysing the local Hartree potential generated by different Ag tip geometries. We considered tetrahedral tips with a one-atom apex (tip-A) and a three-atom apex (tip-B) as shown in Fig. 2a and 2e, respectively.<sup>21</sup> The fields  $\tilde{\Phi}^{\text{tip}}$  were calculated using the Octopus code<sup>44,45</sup> with the LDA exchange-correlation functional (see simulations details in section II in the SI). The use of an arguably small model tip structures to study plasmonic near field distribution from an atomistic first principles perspective is justified by the fact that Ag clusters the plasmon peak is well separated from the interband transitions even for small clusters<sup>46–48</sup>. Fig. 2b and 2f show the magnitude of  $\tilde{\Phi}^{\text{tip}}$  as a function of laser energy and distance from the tip apex, where  $z = 0$  is defined as the center of the nuclei located at the tip apex. In both cases, the maximum  $\tilde{\Phi}^{\text{tip}}$  is found at 1.4 Å below the tip apex and at 3.22 eV. The intensity of the potential decays to its half-value at 4 Å and at 5 Å below the tip apex for tip-A and tip-B, respectively. We analysed larger tip sizes, and verified that the overall shape of  $\tilde{\Phi}^{\text{tip}}$  is not significantly altered and the plasmonic peak approaches the visible range in agreement with previous studies<sup>46</sup> (Fig. S2 in the SI). The two-dimensional cuts of  $\tilde{\Phi}^{\text{tip}}$  for tip-A and tip-B, presented in the remaining panels of Fig. 2, show that the field maximum is found exactly below the apex of tip-A and below the three atoms that constitute the tip apex for tip-B. Interestingly, at 6 Å below the tip apex the shape of  $\tilde{\Phi}^{\text{tip}}$  of the two models becomes indistinguishable, which suggests that for substrate-tip distance greater than 6 Å the fine details of the apex should be negligible in TERS imaging experiments. In passing, we note that at 4 Å below the tip apex the distribution of the local field can be approximated by a 2D Gaussian function to some extent. However a Gaussian profile can neither adequately describe the rapid change of intensity at the center of the distribution nor capture any radial asymmetry (see section III in the SI).

We proceed by computing TERS spectra for the free-standing benzene molecule. Benzene has

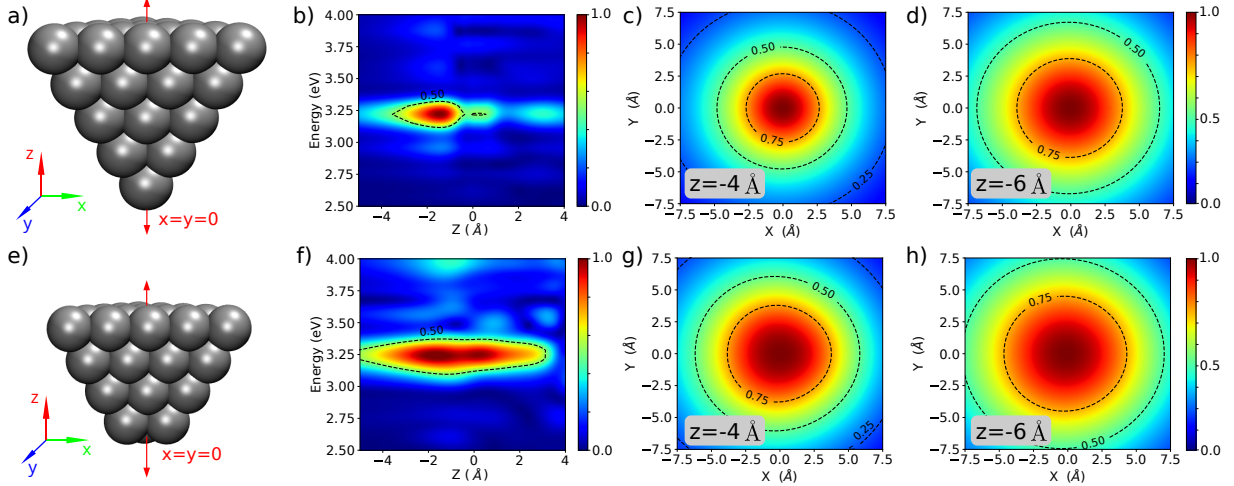


Figure 2: Energy and spatial dependence of the tip Hartree potential from TDDFT simulations. Panel a) shows the structure of tip-A model. Panel b) shows the normalized  $\tilde{\Phi}^{\text{tip}}$  along the  $(x = 0, y = 0, z)$  line. Panels c) and d) show normalized two dimensional cuts at 3.22 eV and  $z$  equal to 4 Å, and 6 Å below the tip apex. Panels f)–h) are analogous to panels a)–d) for the tip-B model. In all plots the origin is defined at the tip apex position.

been investigated several times as a proof-of-concept molecule<sup>25,28</sup> and it allows us to compare the current method with others proposed in the literature. We calculated Raman intensities with the FHI-aims<sup>49</sup> code and the LDA functional, where the DFPT implementation<sup>50</sup> has been extended to include the local field as prescribed by Eq. 3 and to account for plasmonic terms in the electronic-density response of metallic clusters. We consider a benzene molecule in a flat orientation, as depicted in Fig. 3a, and compute the TERS spectra for different tip-molecule distances,  $d$ , as shown in Fig. 3b. In these calculations, tip-A was used and its apex was aligned to center of the benzene molecule. We remark that only the signal coming from the  $\alpha_{zz}$  component of the polarizability tensor is shown. By analyzing the projected density of states of the benzene-tip system (see SI section III) we concluded that for distances larger than 3 Å, the assumption that there is no chemical interaction between the two subsystems is valid. Moreover, by analyzing the molecular induced dipole at different tip-molecule relative positions, we verified that at these molecule-tip distances, we are within the applicability realm of first-order perturbation theory (see SI section III).

The inhomogeneity of the local field induces changes in the TERS spectra in two distinctive

ways when compared to the standard (homogeneous field) Raman spectrum. On one hand, the intensity of the peaks at 1015 and 3121  $\text{cm}^{-1}$  ( $a_{1g}$ ), is enhanced with respect to the homogeneous field case. On the other hand, the  $a_{2u}$  mode at 654  $\text{cm}^{-1}$  which is Raman inactive becomes active in the TERS spectrum, which denotes a new selection rule arising from the spatial variation of the local field. In Fig. 3 panels c)-e), we show the normal mode eigenvectors of selected vibrational modes, and in panels f)-h), their corresponding TERS images. The images were obtained by computing the TERS spectra at different lateral positions of the tip with respect to the molecule, at a constant height of 4 Å. The intensities of the corresponding vibrational mode were then plotted in a two-dimensional heat map. The images of the modes located at 828  $\text{cm}^{-1}$  and 3121  $\text{cm}^{-1}$  show distinctive patterns that are comparable to the ones obtained by Jensen and coworkers with a more phenomenological approach.<sup>25</sup> Our prediction for the mode located at 654  $\text{cm}^{-1}$  shows a circular spot located with the highest intensity at the center of the benzene molecule, which contrasts with the image reported by Jensen in which six well-defined spots appear centred at the hydrogen positions. We attribute this difference to the artificially narrow width used to describe the local field in their phenomenological approach, as well as the unphysical short distance considered between the local field and the molecule. Indeed, by carefully adjusting these parameters in their modelling, a similar image to the one presented in this work can be obtained (see SI in Ref. 25). This example demonstrates the importance of employing a parameter-free method, with easy-to-verify assumptions, that can deliver results without adjustable parameters.

Finally, we consider the tetracyanoethylene (TCNE) molecule as a representative molecule that strongly interacts with metallic adsorbates.<sup>51</sup> TCNE is a strong electron acceptor due to the four cyano-groups low-energy orbitals conjugated to the central C-C bond,<sup>52</sup> and has been investigated as a room temperature molecular magnet.<sup>53</sup> To study the impact of chem-GS enhancements on TERS spectra, we consider three scenarios: i) The TCNE molecule with its optimized geometry in the gas phase (TCNE<sub>gas</sub>), ii) the molecule adsorbed on Ag(110) (TCNE@Ag(110)), and iii) the molecule in the gas-phase but fixed at the adsorbed geometry (TCNE<sub>ads</sub>). The Ag(110) surface was modeled by a 3-layer 4×4 cluster and we employed the PBE functional in our DFPT

calculations (see more details and convergence tests in the section II of the SI).

TCNE is a planar molecule in the gas-phase. Upon adsorption with a flat orientation, the TCNE molecule arcs with the CN groups pointing toward the Ag atoms (see Fig. 4a), and gets negatively charged producing an elongation of the central C-C bond.<sup>52</sup> The TCNE<sub>gas</sub>, TCNE<sub>Eads</sub> and TCNE@Ag(110) TERS spectra, calculated according to Eq. 4, are presented in Fig. 4b with black, orange and red curves, respectively. The TCNE<sub>gas</sub> spectrum presents three main peaks. The ones at 144 cm<sup>-1</sup> and 557 cm<sup>-1</sup> correspond to out-of-plane modes while the vibrations at 2239 cm<sup>-1</sup> corresponds to the in-plane CN stretching mode. The TCNE<sub>Eads</sub> spectrum also presents three major peaks at 207 cm<sup>-1</sup>, 555 cm<sup>-1</sup>, and 2119 cm<sup>-1</sup>, which correspond to equivalent vibrational modes. However, due to the deformation of the molecular geometry, some of the vibrational frequencies are considerably red or blue shifted. In addition, this spectrum presents several satellite peaks of relative low intensity. The TCNE@Ag(110) spectrum is around two orders of magnitude more intense than the other spectra due to chem-GS enhancement. While the peak at 2127 cm<sup>-1</sup> preserves the CN stretch character and is considerably enhanced, the modes around 200 cm<sup>-1</sup> and 550 cm<sup>-1</sup> get mixed with other normal modes and show a relatively smaller intensity enhancement. A new high-intensity peak appears at 1235 cm<sup>-1</sup> and corresponds to the central C-C stretching mode.

In the remaining panels in Fig. 4, we present the TERS images for selected vibrational modes. To make a legit comparison, and to isolate the effect caused by chem-GS enhancement, we only compare TCNE<sub>Eads</sub> with TCNE@Ag(110) (same molecular geometry), and in the evaluation of Eq. 4, we use the normal modes associated to the TCNE@Ag(110) structure. The TERS images of the central C-C stretching mode are shown in panels d) and e) and present comparable shapes with most of the Raman signal localized in the vicinity of the molecular center. However, the TCNE<sub>Eads</sub> image shows two clearly separated spots with the highest intensity at each side of the molecule along the central C-C bond axis. The intensity at the center of the molecule is relatively small, as shown in the 1D spectra. In panels, g-h), j-k), and m-n) we present other vibrational modes that show TERS activity, including out-of-plane and in-plane molecular motions. The TERS images

when including the Ag atoms are remarkably different even though we are considering the same geometry and nuclear displacements in the calculations. This observation proves that the symmetry of the normal modes does not exclusively determine TERS images and chem-GS effects can play a decisive role in determining the shape and intensity of the image. Moreover, neither a normal mode analysis nor a simple symmetry argument, or a frequency comparison between TCNEads and TCNE@Ag(110) calculations, seem to be able to predict a priori the impact of the chem-GS enhancement on the shape of the TERS images. We also verified that adding a negative charge to the TCNEads calculations does not reproduce the TCNE@Ag(110) results (see Fig. S12 in the SI). This highlights once again the necessity of a first-principles calculation including the substrate.

In summary, we have presented a new first-principles method to compute TERS spectra and images, that retains computational efficiency. The method does not rely on simplistic models for the tip geometry and its generated field, and is able to capture EM and chem-GS types of Raman signal enhancement. Therefore, it enables the calculation of TERS spectra and images for system sizes well beyond the current capabilities of real-time TDDFT simulations.<sup>54,55</sup> We presented results for two molecules: One that physisorbs on metallic substrates (benzene) and another that chemisorbs (TCNE). For the former case, we showed that the predicted TERS images differ from simplified approaches unless specific parameters are calibrated. For the latter, we showed that the chemical interaction between the molecule and the substrate leads to drastic changes in the TERS images which reveal that the chemical enhancement shows atomic-scale variation. The accuracy of the method we propose remains to be fully benchmarked, since a reference theoretical TERS calculation including all effects of light-matter coupling in the semiclassical limit,<sup>56,57</sup> has not yet been reported in literature. Nevertheless, this method bridges an important gap in terms of accuracy and computational cost among existing approaches of TERS simulations, facilitating the interpretation of TERS experiments for realistic complex systems. We hope that the reported results motivate new single-molecule TERS experiments on inorganic/organic hybrid interfaces composed of chemisorbed molecules relevant to electronic and light-harvesting applications<sup>58–60</sup>.

## Acknowledgement

The authors wish to acknowledge the support of the Max Planck Society. Y.L. has been partly funded by the Deutsche Forschungsgemeinschaft (DFG, German Research Foundation) project number 467724959. F.P.B. acknowledges financial support from the European Union's Horizon 2020 research and innovation programme under the Marie Skłodowska-Curie Grant Agreement no. 895747 (NanoLightQD). M.R. and A.A. acknowledge funding by the Deutsche Forschungsgemeinschaft (DFG) – Projektnummer 182087777 – SFB 951. Y.L. would like to thank Oliver Hofmann for suggesting the investigation of the TCNE molecule in this project and Thomas Purcell for a critical reading of the manuscript.

## Supporting Information Available

See supporting information for a detailed derivation of Eq. 3, further computational details, and validation tests. A tutorial to generate TERS images for the benzene molecule with the FHI-aims code with all the necessary input files is available at [https://github.com/sabia-group/TERS\\_Tutorial](https://github.com/sabia-group/TERS_Tutorial)

## References

- (1) Gross, L. Recent advances in submolecular resolution with scanning probe microscopy. *Nat. Chem.* **2011**, *3*, 273–278.
- (2) Lee, J.; Crampton, K. T.; Tallarida, N.; Apkarian, V. A. Visualizing vibrational normal modes of a single molecule with atomically confined light. *Nature* **2019**, *568*, 78–82.
- (3) Hayazawa, N.; Inouye, Y.; Sekkat, Z.; Kawata, S. Metallized tip amplification of near-field Raman scattering. *Opt. Commun.* **2000**, *183*, 333–336.

- (4) Anderson, M. S. Locally enhanced Raman spectroscopy with an atomic force microscope. *Appl. Phys. Lett.* **2000**, *76*, 3130–3132.
- (5) Stöckle, R. M.; Suh, Y. D.; Deckert, V.; Zenobi, R. Nanoscale chemical analysis by tip-enhanced Raman spectroscopy. *Chem. Phys. Lett.* **2000**, *318*, 131–136.
- (6) Steidtner, J.; Pettinger, B. Tip-Enhanced Raman Spectroscopy and Microscopy on Single Dye Molecules with 15 nm Resolution. *Phys. Rev. Lett.* **2008**, *100*, 236101.
- (7) Zrimsek, A. B.; Chiang, N.; Mattei, M.; Zaleski, S.; McAnally, M. O.; Chapman, C. T.; Henry, A.-I.; Schatz, G. C.; Van Duyne, R. P. Single-Molecule Chemistry with Surface- and Tip-Enhanced Raman Spectroscopy. *Chem. Rev.* **2017**, *117*, 7583–7613.
- (8) Chulhai, D. V.; Hu, Z.; Moore, J. E.; Chen, X.; Jensen, L. Theory of Linear and Nonlinear Surface-Enhanced Vibrational Spectroscopies. *Annu. Rev. Phys. Chem.* **2016**, *67*, 541–564.
- (9) Zhang, R.; Zhang, Y.; Dong, Z. C.; Jiang, S.; Zhang, C.; Chen, L. G.; Zhang, L.; Liao, Y.; Aizpurua, J.; Luo, Y.; Yang, J. L.; Hou, J. G. Chemical mapping of a single molecule by plasmon-enhanced Raman scattering. *Nature* **2013**, *498*, 82–86.
- (10) van Schrojenstein Lantman, E. M.; Deckert-Gaudig, T.; Mank, A. J. G.; Deckert, V.; Weckhuysen, B. M. Catalytic processes monitored at the nanoscale with tip-enhanced Raman spectroscopy. *Nature Nanotechnol.* **2012**, *7*, 583–586.
- (11) Sun, M.; Zhang, Z.; Zheng, H.; Xu, H. In-situ plasmon-driven chemical reactions revealed by high vacuum tip-enhanced Raman spectroscopy. *Sci. Rep.* **2012**, *2*, 647.
- (12) Farhat, P.; Avilés, M. O.; Legge, S.; Wang, Z.; Sham, T.-K.; Lagugné-Labarthe, F. Tip-Enhanced Raman Spectroscopy and Tip-Enhanced Photoluminescence of MoS<sub>2</sub> Flakes Decorated with Gold Nanoparticles. *J. Phys. Chem. C* **2022**, *126*, 7086–7095.
- (13) Birmingham, B.; Liege, Z.; Larson, N.; Lu, W.; Park, K. T.; Lee, H. W. H.; Voronine, D. V.;

- Scully, M. O.; Zhang, Z. Probing Interaction between Individual Submonolayer Nanoislands and Bulk MoS<sub>2</sub> Using Ambient TERS. *J. Phys. Chem. C* **2018**, *122*, 2753–2760.
- (14) Rahaman, M.; Rodriguez, R. D.; Plechinger, G.; Moras, S.; Schüller, C.; Korn, T.; Zahn, D. R. T. Highly Localized Strain in a MoS<sub>2</sub>/Au Heterostructure Revealed by Tip-Enhanced Raman Spectroscopy. *Nano Lett.* **2017**, *17*, 6027–6033.
- (15) Martín Sabanés, N.; Ohto, T.; Andrienko, D.; Nagata, Y.; Domke, K. F. Electrochemical TERS Elucidates Potential-Induced Molecular Reorientation of Adenine/Au(111). *Angew. Chem. Int. Ed.* **2017**, *56*, 9796–9801.
- (16) Zeng, Z.-C.; Huang, S.-C.; Wu, D.-Y.; Meng, L.-Y.; Li, M.-H.; Huang, T.-X.; Zhong, J.-H.; Wang, X.; Yang, Z.-L.; Ren, B. Electrochemical Tip-Enhanced Raman Spectroscopy. *J. Am. Chem. Soc.* **2015**, *137*, 11928–11931.
- (17) Jensen, L.; Aikens, C. M.; Schatz, G. C. Electronic structure methods for studying surface-enhanced Raman scattering. *Chem. Soc. Rev.* **2008**, *37*, 1061–1073.
- (18) Zhang, C.; Chen, B.-Q.; Li, Z.-Y. Optical Origin of Subnanometer Resolution in Tip-Enhanced Raman Mapping. *J. Phys. Chem. C* **2015**, *119*, 11858–11871.
- (19) Fiederling, K.; Kupfer, S.; Gräfe, S. Are charged tips driving TERS-resolution? A full quantum chemical approach. *J. Chem. Phys.* **2021**, *154*, 034106.
- (20) Latorre, F.; Kupfer, S.; Bocklitz, T.; Kinzel, D.; Trautmann, S.; Gräfe, S.; Deckert, V. Spatial resolution of tip-enhanced Raman spectroscopy – DFT assessment of the chemical effect. *Nanoscale* **2016**, *8*, 10229–10239.
- (21) Cirera, B.; Litman, Y.; Lin, C.; Akkoush, A.; Hammud, A.; Wolf, M.; Rossi, M.; Kumagai, T. Charge Transfer-Mediated Dramatic Enhancement of Raman Scattering upon Molecular Point Contact Formation. *Nano Lett.* **2022**, *22*, 2170–2176.

- (22) Aiga, N.; Takeuchi, S. Single-Molecule Raman Spectroscopy of a Pentacene Derivative Adsorbed on the Nonflat Surface of a Metallic Tip. *J. Phys. Chem. C* **2022**, *126*, 16227–16235.
- (23) Giesecking, R. L. M.; Lee, J.; Tallarida, N.; Apkarian, V. A.; Schatz, G. C. Bias-Dependent Chemical Enhancement and Nonclassical Stark Effect in Tip-Enhanced Raman Spectromicroscopy of CO-Terminated Ag Tips. *J. Phys. Chem. Lett.* **2018**, *9*, 3074–3080.
- (24) Yang, B.; Chen, G.; Ghafoor, A.; Zhang, Y.-F.; Zhang, X.-B.; Li, H.; Dong, X.-R.; Wang, R.-P.; Zhang, Y.; Zhang, Y.; Dong, Z.-C. Chemical Enhancement and Quenching in Single-Molecule Tip-Enhanced Raman Spectroscopy. *Angew. Chem. Int. Ed. (2013, in press)* **2023**, *in press*.
- (25) Chen, X.; Liu, P.; Hu, Z.; Jensen, L. High-resolution tip-enhanced Raman scattering probes sub-molecular density changes. *Nature Comm.* **2019**, *10*, 2567.
- (26) Duan, S.; Tian, G.; Luo, Y. Visualization of Vibrational Modes in Real Space by Tip-Enhanced Non-Resonant Raman Spectroscopy. *Angew. Chem. Int. Ed.* **2016**, *55*, 1041–1045.
- (27) Iwasa, T.; Nobusada, K. Nonuniform light-matter interaction theory for near-field-induced electron dynamics. *Phys. Rev. A* **2009**, *80*, 043409.
- (28) Takenaka, M.; Taketsugu, T.; Iwasa, T. Theoretical method for near-field Raman spectroscopy with multipolar Hamiltonian and real-time-TDDFT: Application to on- and off-resonance tip-enhanced Raman spectroscopy. *J. Chem. Phys.* **2021**, *154*, 024104.
- (29) Chen, H.; McMahon, J. M.; Ratner, M. A.; Schatz, G. C. Classical Electrodynamics Coupled to Quantum Mechanics for Calculation of Molecular Optical Properties: a RT-TDDFT/FDTD Approach. *J. Phys. Chem. C* **2010**, *114*, 14384–14392.
- (30) Payton, J. L.; Morton, S. M.; Moore, J. E.; Jensen, L. A Hybrid Atomistic Electrodynamics–Quantum Mechanical Approach for Simulating Surface-Enhanced Raman Scattering. *Acc. Chem. Res.* **2014**, *47*, 88–99.

- (31) Duan, S.; Tian, G.; Ji, Y.; Shao, J.; Dong, Z.; Luo, Y. Theoretical Modeling of Plasmon-Enhanced Raman Images of a Single Molecule with Subnanometer Resolution. *J. Am. Chem. Soc.* **2015**, *137*, 9515–9518.
- (32) Liu, P.; Chulhai, D. V.; Jensen, L. Single-Molecule Imaging Using Atomistic Near-Field Tip-Enhanced Raman Spectroscopy. *ACS Nano* **2017**, *11*, 5094–5102.
- (33) Zhang, P.; Feist, J.; Rubio, A.; García-González, P.; García-Vidal, F. J. Ab initio nanoplasmonics: The impact of atomic structure. *Phys. Rev. B* **2014**, *90*, 1–5.
- (34) Barbry, M.; Koval, P.; Marchesin, F.; Esteban, R.; Borisov, A. G.; Aizpurua, J.; Sánchez-Portal, D. Atomistic near-field nanoplasmonics: Reaching atomic-scale resolution in nanooptics. *Nano Lett.* **2015**, *15*, 3410–3419.
- (35) Urbietta, M.; Barbry, M.; Zhang, Y.; Koval, P.; Sánchez-Portal, D.; Zabala, N.; Aizpurua, J. Atomic-Scale Lightning Rod Effect in Plasmonic Picocavities: A Classical View to a Quantum Effect. *ACS Nano* **2018**, *12*, 585–595.
- (36) Zhu, W.; Esteban, R.; Borisov, A. G.; Baumberg, J. J.; Nordlander, P.; Lezec, H. J.; Aizpurua, J.; Crozier, K. B. Quantum mechanical effects in plasmonic structures with subnanometre gaps. *Nat. Comm.* **2016**, *7*, 11495.
- (37) Marques, M. A.; Ullrich, C. A.; Nogueira, F.; Rubio, A.; Burke, K.; Gross, E. K. *Time-dependent density functional theory*; Springer Science & Business Media, 2006; Vol. 706.
- (38) Long, D. A. *The Raman Effect*; John Wiley and Sons, Inc, 2002.
- (39) Ross-Murphy, S. B. Dynamic Light Scattering. B. J. Berne and R. Pecora, John Wiley, New York, 1976. *Br. Polym. J.* **1977**, *9*, 177–177.
- (40) Raimbault, N.; Athavale, V.; Rossi, M. Anharmonic effects in the low-frequency vibrational modes of aspirin and paracetamol crystals. *Phys. Rev. Mat.* **2019**, *3*, 053605.

- (41) Peller, D.; Roelcke, C.; Kastner, L. Z.; Buchner, T.; Neef, A.; Hayes, J.; Bonafé, F.; Sidler, D.; Ruggenthaler, M.; Rubio, A.; Huber, R.; Repp, J. Quantitative sampling of atomic-scale electromagnetic waveforms. *Nature Photon.* **2021**, *15*, 143–147.
- (42) Chulhai, D. V.; Jensen, L. Determining Molecular Orientation With Surface-Enhanced Raman Scattering Using Inhomogeneous Electric Fields. *J. Phys. Chem. C* **2013**, *117*, 19622–19631.
- (43) Gersten, J.; Nitzan, A. Electromagnetic theory of enhanced Raman scattering by molecules adsorbed on rough surfaces. *J. Chem. Phys.* **1980**, *73*, 3023–3037.
- (44) Andrade, X. et al. Real-space grids and the Octopus code as tools for the development of new simulation approaches for electronic systems. *Phys. Chem. Chem. Phys.* **2015**, *17*, 31371–31396.
- (45) Tancogne-Dejean, N. et al. Octopus, a computational framework for exploring light-driven phenomena and quantum dynamics in extended and finite systems. *J. Chem. Phys.* **2020**, *152*, 124119.
- (46) Douglas-Gallardo, O. A.; Berdakin, M.; Frauenheim, T.; Sánchez, C. G. Plasmon-induced hot-carrier generation differences in gold and silver nanoclusters. *Nanoscale* **2019**, *11*, 8604–8615.
- (47) Negre, C. F. A.; Perassi, E. M.; Coronado, E. a.; Sánchez, C. G. Quantum dynamical simulations of local field enhancement in metal nanoparticles. *J. Phys. Condens. Matter* **2013**, *25*, 125304.
- (48) Bonafé, F. P.; Aradi, B.; Guan, M.; Douglas-Gallardo, O. A.; Lian, C.; Meng, S.; Frauenheim, T.; Sánchez, C. G. Plasmon-driven sub-picosecond breathing of metal nanoparticles. *Nanoscale* **2017**, *9*, 12391–12397.

- (49) Blum, V.; Gehrke, R.; Hanke, F.; Havu, P.; Havu, V.; Ren, X.; Reuter, K.; Scheffler, M. Ab initio molecular simulations with numeric atom-centered orbitals. *Comp. Phys. Comm.* **2009**, *180*, 2175 – 2196.
- (50) Shang, H.; Raimbault, N.; Rinke, P.; Scheffler, M.; Rossi, M.; Carbogno, C. All-electron, real-space perturbation theory for homogeneous electric fields: theory, implementation, and application within DFT. *New J. Phys.* **2018**, *20*, 073040.
- (51) Wegner, D.; Yamachika, R.; Zhang, X.; Wang, Y.; Crommie, M. F.; Lorente, N. Adsorption Site Determination of a Molecular Monolayer via Inelastic Tunneling. *Nano Lett.* **2013**, *13*, 2346–2350.
- (52) Miller, J. S. Tetracyanoethylene (TCNE): The Characteristic Geometries and Vibrational Absorptions of Its Numerous Structures. *Angew. Chem. Int. Ed.* **2006**, *45*, 2508–2525.
- (53) Manriquez, J. M.; Yee, G. T.; McLean, R. S.; Epstein, A. J.; Miller, J. S. A Room-Temperature Molecular/Organic-Based Magnet. *Science* **1991**, *252*, 1415–1417.
- (54) Zhao,.; Jensen, L.; Schatz, G. C. Pyridine Ag<sub>20</sub> Cluster: A Model System for Studying Surface-Enhanced Raman Scattering. *J. Am. Chem. Soc.* **2006**, *128*, 2911–2919.
- (55) Tsuneda, T.; Iwasa, T.; Taketsugu, T. Roles of silver nanoclusters in surface-enhanced Raman spectroscopy. *J. Chem. Phys.* **2019**, *151*, 094102.
- (56) Jestädt, R.; Ruggenthaler, M.; Oliveira, M. J. T.; Rubio, A.; Appel, H. Light-matter interactions within the Ehrenfest–Maxwell–Pauli–Kohn–Sham framework: fundamentals, implementation, and nano-optical applications. *Adv. Phys.* **2019**, *68*, 225–333.
- (57) Flick, J.; Rivera, N.; Narang, P. Strong light-matter coupling in quantum chemistry and quantum photonics. *Nanophotonics* **2018**, *7*, 1479–1501.
- (58) Wang, H.; Levchenko, S. V.; Schultz, T.; Koch, N.; Scheffler, M.; Rossi, M. Modulation of the

Work Function by the Atomic Structure of Strong Organic Electron Acceptors on H-Si(111). *Adv. Electron. Mater.* **2019**, *5*, 1800891.

- (59) Riede, M.; Mueller, T.; Tress, W.; Schueppel, R.; Leo, K. Small-molecule solar cells—status and perspectives. *Nanotechnology* **2008**, *19*, 424001.
- (60) Zhang, F.; Kahn, A. Investigation of the High Electron Affinity Molecular Dopant F6-TCNNQ for Hole-Transport Materials. *Adv. Funct. Mater.* **2018**, *28*, 1703780.

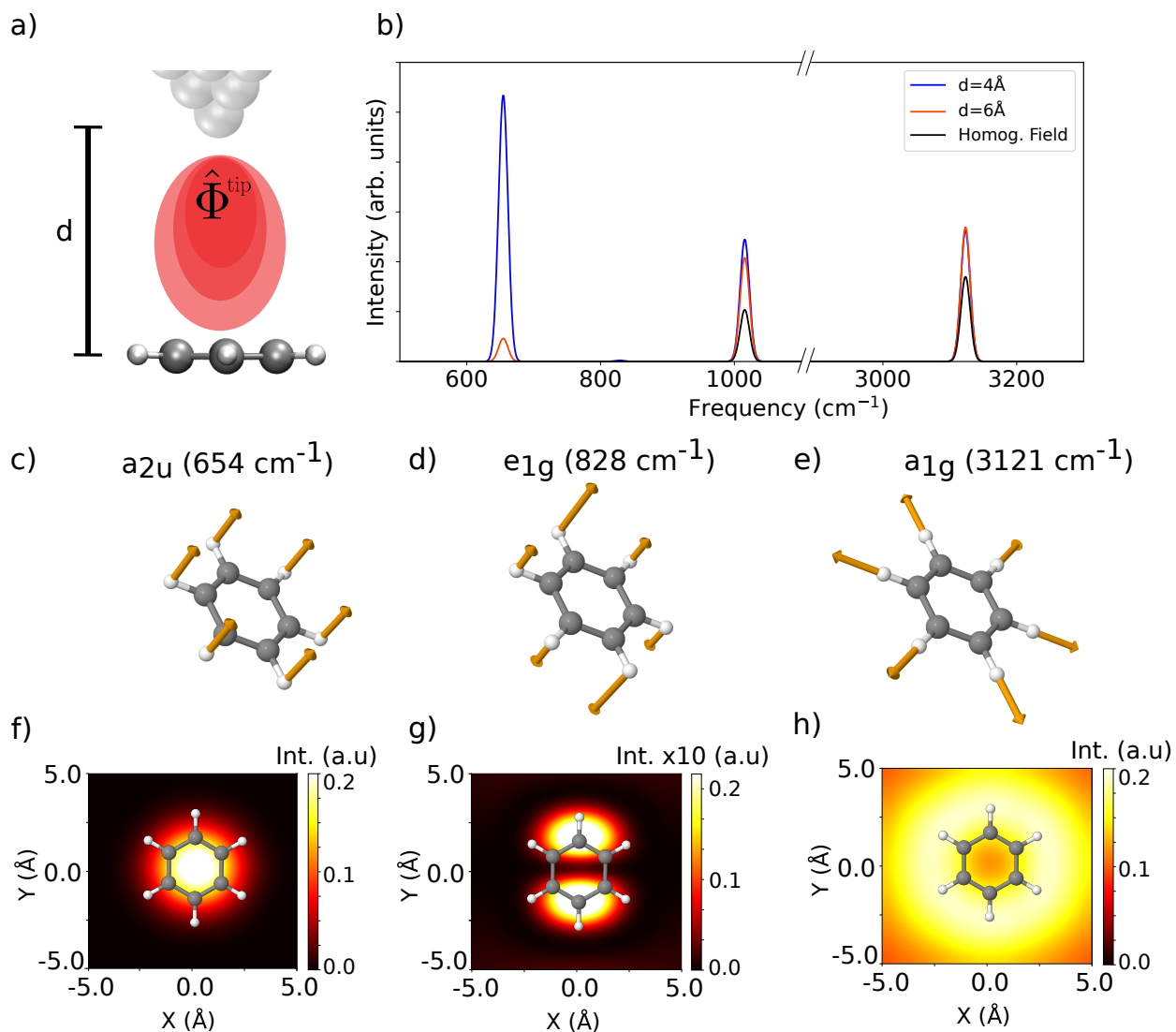


Figure 3: TERS simulation of gas-phase benzene from local-field DFPT calculations. a) Sketch of simulation setup. b) Simulated harmonic TERS spectrum of the benzene molecule for different tip-molecule distances,  $d$ , compared to the homogeneous-field case. Only the signal coming from the  $\alpha_{zz}$  component is shown for all cases. The observed enhancement is non-linear with the molecule-tip distance since higher-order derivatives of the local potential start to contribute to the signal at the shortest distances.<sup>42</sup> c-e) Normal mode eigenvectors of selected vibrational modes with their respective symmetries and frequencies. f-h) TERS images of the selected vibrational modes for a molecule-tip apex distance of  $4 \text{\AA}$ . See Fig. S11 in the SI for the TERS image of the  $1015 \text{ cm}^{-1}$  peak.

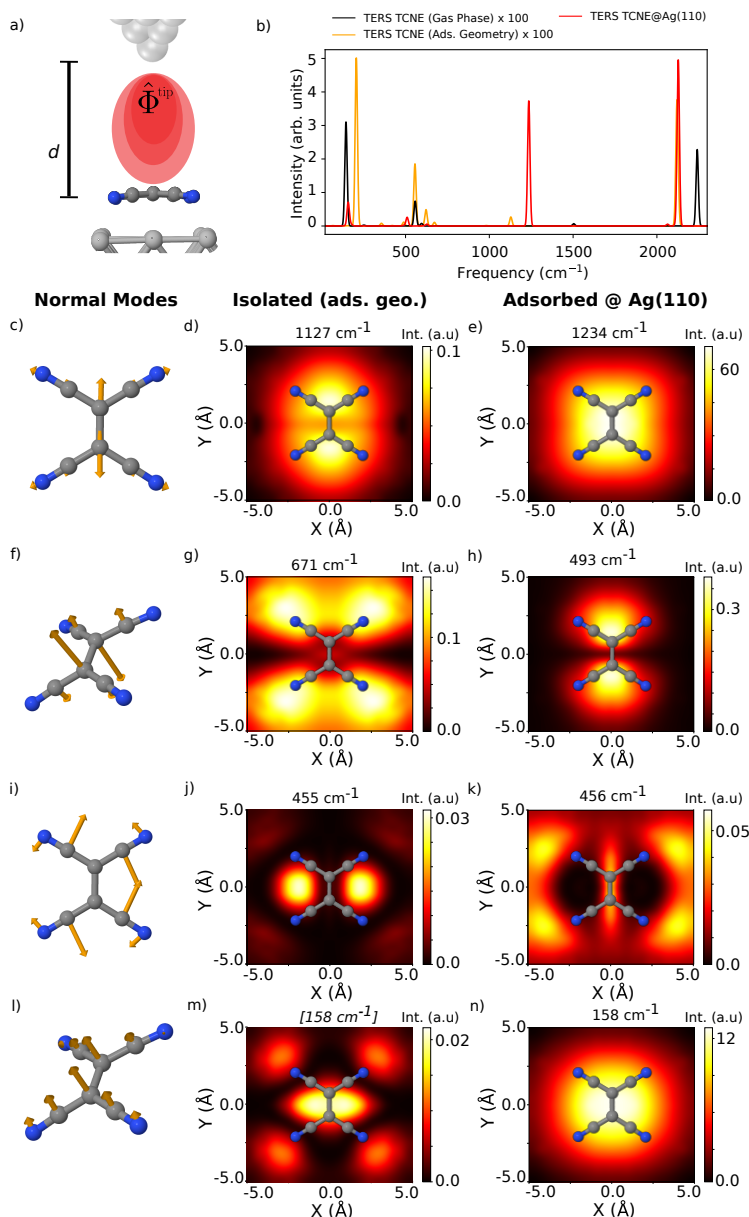
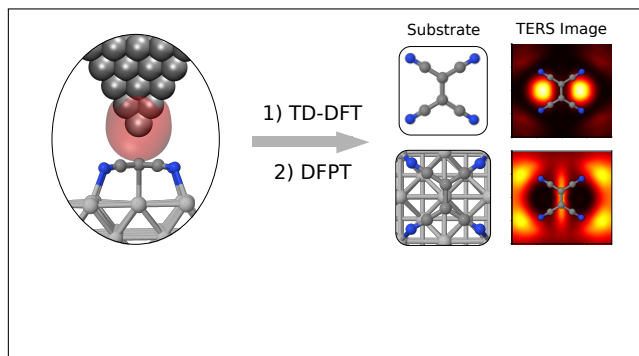


Figure 4: a) Sketch of simulation setup of TCNE adsorbed on an Ag(110) cluster. b) Simulated TERS image of TCNE in isolation (TCNE<sub>gas</sub>, black), of TCNE in isolation, but at the adsorbed geometry (TCNE<sub>ads</sub>, orange), and of TCNE at the Ag(110) cluster discussed in the text (TCNE@Ag(110), red). Tip apex was placed on the molecular center of mass at a distance of 4 Å. c), f), i) and l) Normal mode displacement vectors of selected vibrational modes of TCNE@Ag(110). The surface has been deleted for clarity. d), g), j) and m) TERS images of the depicted normal modes for TCNE<sub>ads</sub>. e), h), k) and n) TERS images of the depicted normal modes for TCNE@Ag(110). In all cases a molecule-apex distance of 4 Å was employed. Frequency within square brackets in panel m) denotes the lack of an equivalent normal mode eigenvector in the TCNE<sub>ads</sub> calculation.

# Graphical TOC Entry



## Supplemental Information: First-Principles Simulations of Tip Enhanced Raman Scattering Reveal Active Role of Substrate on High-Resolution Images

Y. Litman,<sup>1,2,3, a)</sup> F. Bonafe,<sup>2,3</sup> A. Akkoush,<sup>2,4</sup> H. Appel,<sup>2</sup> and M. Rossi<sup>2,4</sup>

<sup>1)</sup> *Yusuf Hamied Department of Chemistry, University of Cambridge, Lensfield Road, Cambridge, CB2 1EW, UK*

<sup>2)</sup> *MPI for the Structure and Dynamics of Matter, Luruper Chaussee 149, 22761 Hamburg, Germany*

<sup>3)</sup> *These authors contributed equally*

<sup>4)</sup> *Fritz Haber Institute of the Max Planck Society, Faradayweg 4–6, 14195 Berlin, Germany*

(Dated: 8 March 2023)

---

<sup>a)</sup> Electronic mail: yl899@cam.ac.uk

## I. THEORY

### A. Systems in the Presence of a Near Field

Consider a system perturbed by a transverse electromagnetic field. Under the long-wavelength approximation, the system is described by a Hamiltonian of the form

$$\hat{H} = \hat{H}_0 - \hat{\boldsymbol{\mu}} \cdot \mathbf{E}_\perp^n(t), \quad (1)$$

where  $\hat{H}_0$  refers to the unperturbed Hamiltonian,  $\hat{\boldsymbol{\mu}}$  the system dipole operator, and  $\mathbf{E}_\perp^n(t) = (\lambda_x \hat{\mathbf{n}}_x + \lambda_y \hat{\mathbf{n}}_y + \lambda_z \hat{\mathbf{n}}_z) \cos(\omega_0 t)$ , where  $\lambda_{x,y,z}$  are the electromagnetic field strengths and  $\hat{\mathbf{n}}_{x,y,z}$  are unit vectors in each Cartesian direction. For clarity, in the following we consider the perturbation along a particular Cartesian direction  $\alpha$ , since they are separable, but the derivation is easily generalized. Moreover, we consider, for the current derivation, that nuclei are clamped in space.

We shall consider that our system can be divided in two clearly distinguishable parts that we name ‘sm’ (i.e. substrate plus molecule) and tip which allows us to write the Hamiltonian of the full system as

$$\hat{H}_\alpha = \hat{H}_0^{\text{sm}} - \lambda_\alpha \hat{\boldsymbol{\mu}}_\alpha^{\text{sm}} \cos(\omega_0 t) + \hat{H}_0^{\text{tip}} - \lambda_\alpha \hat{\boldsymbol{\mu}}_\alpha^{\text{tip}} \cos(\omega_0 t) + \hat{H}^{\text{int}}, \quad (2)$$

where the label ‘int’ refers to ‘sm-tip’ interaction.

We will assume that the tip is not influenced by the presence of the molecule, which allow us to write a tip Hamiltonian,

$$\hat{H}_\alpha^{\text{tip}} = \hat{H}_0^{\text{tip}} - \lambda_\alpha \hat{\boldsymbol{\mu}}_\alpha^{\text{tip}} \cos(\omega_0 t), \quad (3)$$

and obtain the time-dependent wave function  $|\Psi_\alpha^{\text{tip}}(\mathbf{r}^{\text{tip}}, t)\rangle$  without reference to the molecule subsystem. Moreover, the lack of influence of the molecule on the tip implies that the interaction is purely electrostatic (charge transfer or dispersion are not possible). This approximation is reasonable for neutral molecules and for all but very small tip-molecule distances. Under the previous assumptions the interaction Hamiltonian gets transformed in an effective interaction Hamiltonian,  $\hat{H}^{\text{int,eff}}$  defined as the following expectation value

$$\begin{aligned}
\langle \Psi_\alpha^{\text{tip}}(\mathbf{r}^{\text{tip}}, t; \mathbf{R}^{\text{tip}}) | \hat{H}^{\text{int}}(\mathbf{r}^{\text{tip}}, \mathbf{r}^{\text{sm}}, t) | \Psi_\alpha^{\text{tip}}(\mathbf{r}^{\text{tip}}, t; \mathbf{R}^{\text{tip}}) \rangle &= \hat{H}_\alpha^{\text{int}}(\mathbf{r}^{\text{sm}}, t; \mathbf{R}^{\text{tip}}) \\
&= e \int d\mathbf{r} \frac{\rho_\alpha^{\text{tip}}(\mathbf{r}, t; \mathbf{R}^{\text{tip}})}{|\hat{\mathbf{r}}^{\text{sm}} - \mathbf{r}|} \\
&= e \hat{\Phi}_\alpha^{\text{tip}}(\mathbf{r}^{\text{sm}}, t; \mathbf{R}^{\text{tip}})
\end{aligned} \tag{4}$$

where  $\mathbf{r}_{\text{sm}}$  ( $\mathbf{r}_{\text{tip}}$ ) refers to the position of electrons that belong to the substrate-molecule (tip) subsystem,  $\mathbf{R}_{\text{tip}}$  refers to position of nuclei that belong to the tip subsystem, and the ‘;’ symbol has been used to emphasis the parametric dependence.  $\hat{\Phi}_\alpha^{\text{tip}}(\mathbf{r}, t; \mathbf{R}^{\text{tip}})$  is the time-dependent Hartree potential generated by the tip upon interaction with the  $\alpha$  component of the far field, and it depends on the position operator and parametrically on the coordinates of the tip. It represents the key quantity of the new approach. For reasons that will become clear later, we shall expand the time-dependent Hartree potential around zero field strength,

$$\begin{aligned}
\hat{\Phi}_\alpha^{\text{tip}}(\mathbf{r}, t; \mathbf{R}^{\text{tip}}) &= \hat{\Phi}_\alpha^{\text{tip}}(\mathbf{r}, t; \mathbf{R}^{\text{tip}})|_{\lambda_\alpha=0} + \lambda_\alpha \left. \frac{\partial \hat{\Phi}_\alpha^{\text{tip}}(\mathbf{r}, t; \mathbf{R}^{\text{tip}})}{\partial \lambda_\alpha} \right|_{\lambda_\alpha=0} + O(\lambda^2) \\
&\approx \hat{\Phi}_{\text{GS}}^{\text{tip}}(\mathbf{r}; \mathbf{R}^{\text{tip}}) + \lambda_\alpha \left. \frac{\partial \hat{\Phi}_\alpha^{\text{tip}}(\mathbf{r}, t; \mathbf{R}^{\text{tip}})}{\partial \lambda_\alpha} \right|_{\lambda_\alpha=0}
\end{aligned} \tag{5}$$

where we used the fact that in the absence of an external field the tip is in the electronic ground state (GS). Since we consider a continuous laser and using the fact that linear responses are local in frequency-domain (i.e. the density oscillates predominantly at the frequency of the external field), we can conveniently write

$$\left. \frac{\partial \hat{\Phi}_\alpha^{\text{tip}}(\hat{\mathbf{r}}, t; \mathbf{R}^{\text{tip}})}{\partial \lambda_\alpha} \right|_{\lambda_\alpha=0} = \Re \left[ \left. \frac{\partial \tilde{\Phi}_\alpha^{\text{tip}}(\mathbf{r}, \omega_0; \mathbf{R}^{\text{tip}})}{\partial \lambda_\alpha} \right|_{\lambda_\alpha=0} \right] \cos(\omega_0 t) \tag{6}$$

where  $\tilde{\Phi}^{\text{tip}}$  denotes the Fourier transform the tip Hartree potential. We note that since we are interested in the simulation of time-independent TERS spectroscopy which represents a steady-state excitation, we have the freedom to arbitrarily define the initial time and therefore keep either the real or imaginary part in Eq. 6. However, for later consistency, we have chosen the former and will use this fact later on.

By introducing Eq. 4, 5 and 6 into Eq. 2 and collecting all the terms that depend on the molecular degrees of freedom and are linear on  $\lambda$ , we arrive at the following expression for

the molecular Hamiltonian

$$\begin{aligned}\hat{H}_\alpha^{\text{sm}} &= \hat{H}_0^{\text{sm}} + \hat{H}_\alpha^{\text{int}}(\hat{\mathbf{r}}^{\text{sm}}, t; \mathbf{R}^{\text{tip}}) - \lambda_\alpha \mu_\alpha^{\text{sm}} \cos(\omega_0 t) \\ &= \hat{H}_0^{\text{sm}} + \hat{\Phi}_{\text{GS}}^{\text{tip}}(\mathbf{r}; \mathbf{R}^{\text{tip}}) + \lambda_\alpha \left\{ -\mu_\alpha^{\text{sm}} + \Re \left[ \frac{\partial \tilde{\Phi}_\alpha^{\text{tip}}(\mathbf{r}, \omega_0; \mathbf{R}^{\text{tip}})}{\partial \lambda_\alpha} \Big|_{\lambda_\alpha=0} \right] \right\} \cos(\omega_0 t)\end{aligned}\quad (7)$$

We remark that the previous expression is origin independent and that Eq. 3 presented in the main text represents its *time-independent* version.

## B. Time Independent Density Functional Perturbation Theory

In the framework of Kohn–Sham (KS) DFT, the total energy can be expressed as functional of the electron density,  $\rho$ , as

$$E^{(0)}[\rho] = T_s[\rho] + E_{\text{ext}}[\rho] + E_{\text{H}}[\rho] + E_{\text{xc}}[\rho] + E_{\text{nn}}[\rho] \quad (8)$$

where  $T_s$ ,  $E_{\text{ext}}$ ,  $E_{\text{H}}$ ,  $E_{\text{xc}}$ , and  $E_{\text{nn}}$  are the kinetic energy of non-interacting electrons, the external energy due to the the electron-nuclei electrostatic attraction, the Hartree energy, the exchange-correlation energy, and the nuclei-nuclei electrostatic interaction energy, respectively.

The ground-state total energy is obtained variationally under the constraint that the number of electrons is constant which leads to the Kohn–Sham single-particle equations

$$\hat{h}_{\text{KS}}\psi_p = \epsilon_p\psi_p, \quad (9)$$

where  $\psi_p$  and  $\epsilon_p$  are the KS single particle states and energies, and

$$\hat{h}_{\text{KS}} = \hat{t}_s + \hat{v}_{\text{ext}} + \hat{v}_{\text{H}} + \hat{v}_{\text{xc}} \quad (10)$$

is the KS single particle Hamiltonian. All the terms on the right hand-side of the previous equation are single-particle operators which represent the kinetic energy,  $\hat{t}_s$ , the external potential,  $\hat{v}_{\text{ext}}$ , the Hartree potential,  $\hat{v}_{\text{H}}$  and the exchange-correlation functional,  $\hat{v}_{\text{xc}}$ . The ground-state electronic density is computed by  $\rho_{\text{GS}}(\mathbf{r}) = \sum_p f(\epsilon_p)|\psi_p(\mathbf{r})|^2$  where  $f$  is the occupation function.

We now consider a perturbation due to an external electromagnetic field, in the framework of *time independent* perturbation theory. The energy functional gets an extra term,  $E_E[\rho]$ , and the perturbed KS single-particle Hamiltonian can be expressed as

$$\hat{h}_{\text{KS}}(\epsilon_\alpha) = \hat{h}_{\text{KS}}^{(0)} + \hat{h}_{\text{KS}}^{(1)}\lambda_\alpha + \dots \quad (11)$$

where  $\lambda_\alpha$  is the strength of the external field along the direction  $\alpha$ ,  $\hat{h}_{\text{KS}}^{(1)}$  is the first order response of the Hamiltonian operator given by

$$\hat{h}_{\text{KS}}^{(1)} = +\hat{\nu}_{\text{ext}}^{(1)} + \hat{\nu}_{\text{H}}^{(1)} + \hat{\nu}_{\text{xc}}^{(1)} + \hat{\nu}_{\text{E}}, \quad (12)$$

and  $\hat{\nu}_{\text{E}}^{(1)}$  is the (still not specified) coupling operator between the system and the external electromagnetic field. By introducing analogous expansions for the single-particle states ( $\psi_p = \psi_p^{(0)} + \psi_p^{(1)}\epsilon_\alpha + \dots$ ) and their eigenenergies ( $\epsilon_p = \epsilon_p^{(0)} + \epsilon_p^{(1)}\lambda_\alpha + \dots$ ), one reaches the well-known Sternheimer equation which reads

$$(\hat{h}_{\text{KS}}^{(0)} - \epsilon_0)\psi_p^{(1)} = -(\hat{h}_{\text{KS}}^{(1)} - \epsilon_1)\psi_p^{(0)}. \quad (13)$$

The solution of the Sternheimer equation gives direct access to the density response defined as

$$\rho_\alpha^{(1)}(\mathbf{r}) = \frac{\partial \rho(\mathbf{r})}{\partial \lambda_\alpha} = \sum_p f(\epsilon_p) [\psi_p^{(1)}(\mathbf{r})\psi_p^{(0)}(\mathbf{r}) + \psi_p^{(0)}(\mathbf{r})\psi_p^{(1)}(\mathbf{r})], \quad (14)$$

and allows for the calculation of the induced dipole as

$$\mu_\alpha^{\text{ind}} = \sum_{\beta=1}^3 \lambda_\beta \int d\mathbf{r} \rho_\beta^{(1)}(\mathbf{r}) r_\alpha = \sum_\beta \lambda_\beta \alpha_{\alpha\beta}, \quad (15)$$

in which we identify the components of the polarizability tensor as

$$\alpha_{\alpha\beta} = \frac{\partial \mu_\alpha^{\text{ind}}}{\partial \lambda_\beta} = \int d\mathbf{r} \rho_\beta^{(1)}(\mathbf{r}) r_\alpha. \quad (16)$$

It is central to the following developments that we arrived to Eq. 16 without determining the specific nature of the perturbation,  $\hat{\nu}_{\text{E}}$ , besides the assumption that it is weak enough to allow the omission of electrical non-linear effects. We now consider different suitable forms for  $\hat{\nu}_{\text{E}}$ .

### 1. *Homogeneous Field Perturbation*

In most of the Raman experiments the frequency of the (monochromatic) external electromagnetic field falls in the visible range. In these cases, the field remains approximately constant across the molecular dimensions and it is valid to apply the long-wavelength approximation. Thus, for this homogeneous and time-independent field,  $E_E$  is expressed as

$$E_E[\rho] = -\boldsymbol{\lambda} \cdot \int d\mathbf{r} \rho(\mathbf{r}) \mathbf{r}, \quad (17)$$

and the corresponding single-particle operator becomes

$$\hat{\nu}_E = -\mathbf{r}. \quad (18)$$

### 2. *Linear Field*

The next step towards the inclusion of spatial-dependent fields is to consider a field with a non-vanishing gradient. The extra energy term becomes

$$E_E[\rho] = - \sum_{\alpha} \lambda_{\alpha} \left[ \int d\mathbf{r} \rho(\mathbf{r}) r_{\alpha} - \sum_{\beta} \frac{1}{2} \int d\mathbf{r} \frac{\partial \lambda_{\alpha}}{\partial r_{\beta}} \rho(\mathbf{r}) r_{\alpha} r_{\beta} \right], \quad (19)$$

and the single-particle operator is given by

$$\hat{h}_{\text{KS}}^{(1)} = \hat{\nu}_{\text{ext}}^{(1)} + \hat{\nu}_{\text{H}}^{(1)} + \hat{\nu}_{\text{xc}}^{(1)} - r_{\alpha} - \sum_{\beta} \frac{1}{2} \frac{\partial \lambda_{\alpha}}{\partial r_{\beta}} r_{\alpha} r_{\beta}. \quad (20)$$

It is clear to see that this approach becomes impractical rather quickly if one wants to consider higher-order derivatives. Moreover, if the field is not strictly linear, the previous expression becomes origin dependent since the value of  $\frac{\partial \lambda_{\alpha}}{\partial r_{\beta}}$  is position dependent.

### 3. *Inclusion of Near Fields*

We now consider that the Hamiltonian is given by Eq. 7, but in its *time independent* form. The perturbation up to first order is given by

$$- \mu_{\alpha} + \Re \left[ \frac{\partial \tilde{\Phi}_{\alpha}^{\text{tip}}(\mathbf{r}, \omega_0; \mathbf{R}^{\text{tip}})}{\partial \lambda_{\alpha}} \Big|_{\lambda_{\alpha}=0} \right] \quad (21)$$

and the energy gain can be expressed as

$$E_E[\rho] = \sum_{\alpha} \lambda_{\alpha} \left[ - \int d\mathbf{r} \rho(\mathbf{r}) r_{\alpha} + \int d\mathbf{r} \rho(\mathbf{r}) \Re \left[ \frac{\partial \tilde{\Phi}_{\alpha}^{\text{tip}}(\mathbf{r}, \omega_0; \mathbf{R}^{\text{tip}})}{\partial \lambda_{\alpha}} \Big|_{\lambda_{\alpha}=0} \right] \right]. \quad (22)$$

The first order response of the Hamiltonian operator is given by

$$\hat{h}_{\text{KS}}^{(1)} = \hat{v}_{\text{ext}}^{(1)} + \hat{v}_{\text{H}}^{(1)} + \hat{v}_{\text{xc}}^{(1)} - r_{\alpha} + \Re \left[ \frac{\partial \tilde{\Phi}_{\alpha}^{\text{tip}}(\mathbf{r}, \omega_0; \mathbf{R}^{\text{tip}})}{\partial \lambda_{\alpha}} \Big|_{\lambda_{\alpha}=0} \right]. \quad (23)$$

We note that in this case, the ground-state KS Hamiltonian  $\hat{h}_{\text{KS}}^0$  also gets modified by the addition of the  $\Phi_{\text{GS}}^{\text{tip}}$  term.

### *Summary of approximations and assumptions in the derivation of Eq 7*

What follows is a point-by-point summary of the approximation and assumptions employed in the previous section:

- Eq. 1: Dipole coupling between the system and the far-field.
- Eq. 2: The interaction between the tip and substrate is dictated by classical electrostatics.
- Eq. 3: the tip is not influenced by the presence of the substrate.
- Eq. 5: the external far field strength is small enough, such that the response of the tip lies in the linear regime.
- Eq. 11: the external far field strength is small enough, such that the response of the substrate is linear with respect of the local field strength.

## II. METHODS

### A. DFT and DFPT calculations

All the electronic DFT and DFPT calculations were carried out using FHI-aims code<sup>1</sup> with the 'light' default settings for numerical grids and basis sets. The calculations for benzene molecule were carried out with LDA exchange correlation functional as parameterized by Perdew and Wang<sup>2</sup>. The calculations for the TCNE molecule in the gas phase

and adsorbed on Ag(110) were carried out with the PBE exchange correlation functional instead, to have a better description of the charge transfer between the metal substrate and the molecule. The Ag(110) cluster was modeled by a 3 layers 4 x 4 cluster where only the first two top layers were allowed to relax and the bottom one was kept fixed in their bulk positions. The cluster was created using the atomic simulation environment<sup>3</sup> using a 4.157 Å lattice constant for Ag. The geometries were relaxed within FHI-aims up to a maximum residual force component per atom of 0.005 eV/Å. We compared the projected density of states (PDOS) of the cluster calculations with the ones obtained from periodic calculations using a 3 layer Ag 3x4 slab and k-grid=4x4x1. As shown in Fig. S1, the PDOS of the cluster models is in reasonable agreement with the periodic calculations and markedly different from the gas phase prediction.

The calculation of the Raman intensities were performed by the evaluation of Eq. 3 in the main text by a symmetric finite difference approach. All the atoms in the molecule were displaced by 0.002 Å in all Cartesian directions. All the presented TERS images were computed with 0.5 Å x 0.5 Å resolution after verifying with the benzene molecule that using a 0.25 Å x 0.25 Å resolution doesn't change the image appreciable.

## B. TD-DFT calculations

The real-time TDDFT calculations were carried out with the Octopus code<sup>4,5</sup>, employing the adiabatic local density approximation (ALDA) to describe exchange-correlation effects unless stated otherwise. The field perturbation was introduced by a Dirac delta perturbation in time, also known as 'kick', at the initial time with field strength  $k$ ,  $\mathbf{E} = -\hbar k/e\delta(t)$ , which causes the initial wavefunction to instantaneously acquire a phase factor. We utilized a time step of 0.0065 atomic units of time to integrate the time-dependent Kohn-Sham equations of motion and run the simulations for 30000 steps, saving the Hartree potential every 10 steps in cube file format. We employed field strengths between  $5 \times 10^{-4}$  Å<sup>-1</sup> and  $1.5 \times 10^{-3}$  Å<sup>-1</sup>, and verified to be within the linear-response regime (see Fig. S4). The derivative of  $\Phi^{\text{tip}}$  with respect to the field strength was obtained as

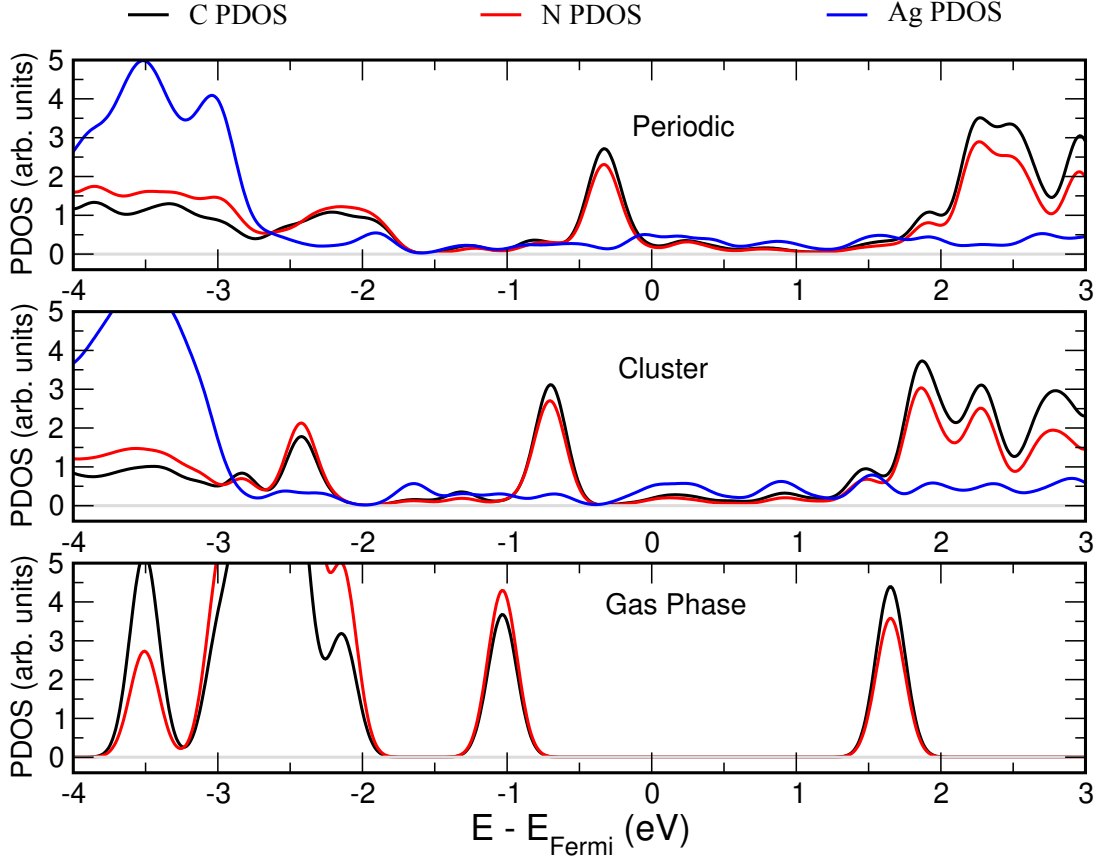


FIG. S1: Projected density of states of TCNE molecule adsorbed at Ag(110) periodic slab (top), TCNE molecule adsorbed at Ag(110) cluster (center), and TCNE molecule in the gas phase (bottom). Carbon, nitrogen and silver atomic PDOS are depicted by black, red and silver curves, respectively. A baseline depicted as a gray curve has been added for clarity in all the panels.

$$\begin{aligned}
 \frac{\partial \tilde{\Phi}^{\text{tip}}(\mathbf{r}, \omega)}{\partial \lambda_{\gamma}^{\text{far}}} &= \frac{\int dt e^{i\omega t} \phi^{\text{tip}}(\mathbf{r}, t)}{\int dt e^{i\omega t} \hbar k / e \delta(t)}, \\
 &= \frac{\int dt e^{i\omega t} \phi^{\text{tip}}(\mathbf{r}, t)}{\hbar k / e}.
 \end{aligned}
 \tag{24}$$

In all the TERS calculations the plasmonic frequency was chosen, i.e.  $\omega = 3.22\text{eV}$ .

### III. VALIDATION TEST

In Fig. S2, we show  $\tilde{\Phi}^{\text{tip}}$  obtained for different tip sizes. The overall shape of  $\tilde{\Phi}^{\text{tip}}$  below

the tip apex is not significantly modified. However, the plasmonic peak approaches the visible range in agreement with previous studies<sup>6</sup>.

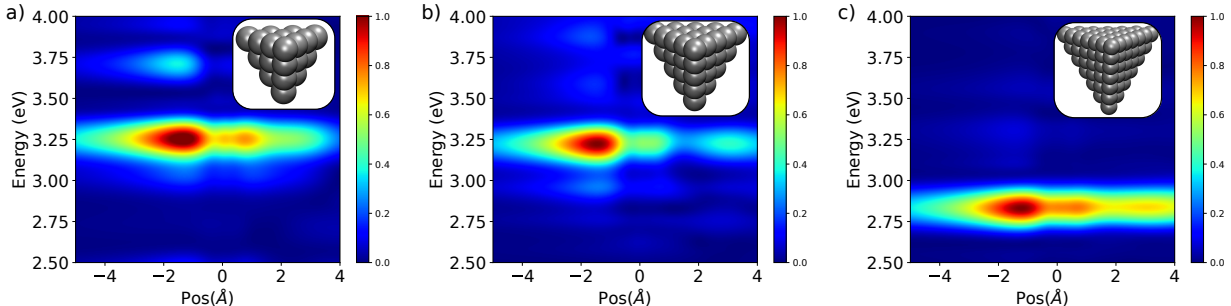


FIG. S2: Comparison  $\tilde{\Phi}_{\text{tip}}$  for different tip sizes. a) Tip smaller than tip-A (20 Ag atoms) b) tip-A (35 Ag atoms) c) Tip bigger than tip-A (84 Ag atoms). The tip apex was set at the origin of coordinates as depicted in Figure 2a in the main text.

In Fig. S3 we show the dependence of  $\tilde{\Phi}_{\text{tip}}$  with respect to the kick strength. At all the considered positions below the the tip apex, a linear dependence is observed

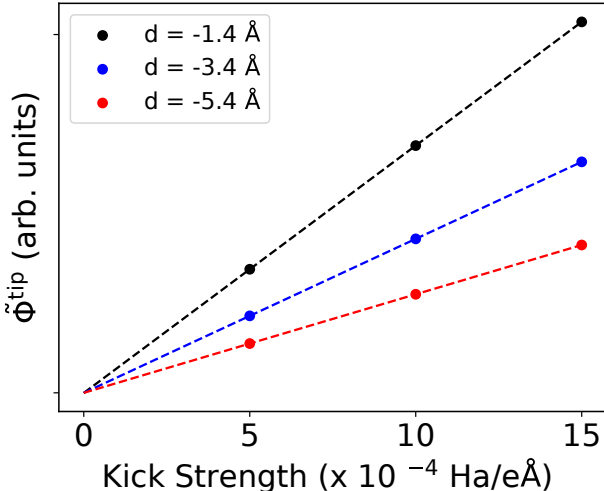


FIG. S3: Linearity of  $\tilde{\Phi}_{\text{tip}}$  with respect to the kick strength. Dots corresponds to  $\tilde{\Phi}_{\text{tip}}$  values at different distances,  $d$ , below the tip apex. Dashed lines are linear fits of the data points.

We studied the dependence of the molecular induced,  $\mu^{\text{ind}}$ , with respect to the kick strength by performing TD-DFT simulations with a kick for a system composed of tipA and a benzene molecule at 4 Å below it. Fig. S4a shows the three different tip-molecule relative positions considered for this test. To isolate the molecular contribution from the

much larger tip contribution, we computed  $\mu^{\text{ind}}$  by integrating a region containing only the molecule (see Fig. S4b) We verified that in this region, the electronic density integrates to the number of electrons in the molecule. In Fig. S4, we show the dependence of  $\mu^{\text{ind}}$  with respect to the kick strength and find a linear dependence. This confirms that we are within the applicability realm of first-order perturbation theory. Moreover, the change of intensity of the induced dipole follows the same trend as the TERS image presented in the main text (see Fig3 g) with a maximum at  $d=2.5\text{\AA}$ .

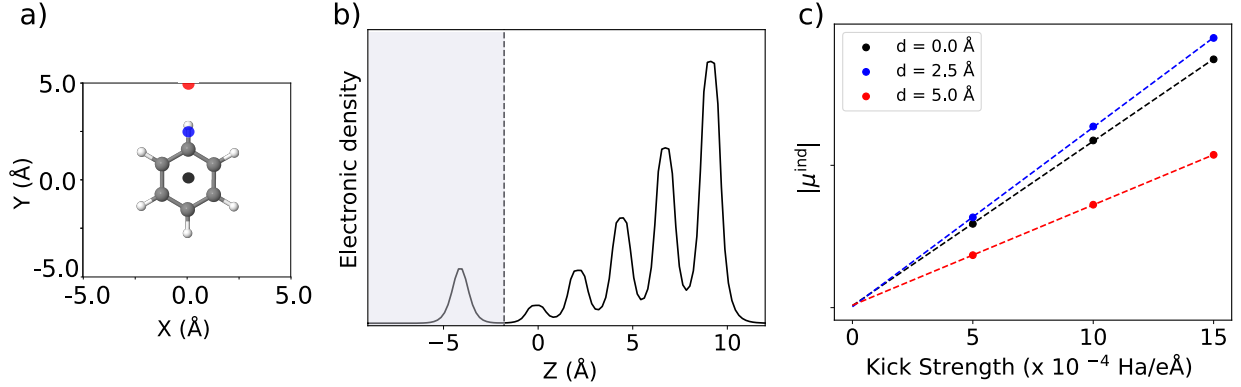


FIG. S4: a) Visual representation of the benzene molecule and the the 3 lateral positions of the tip apex considered for this test. b) Electronic density along the z-direction (main tip axis) integrated along the orthogonal xy plane. Molecular induced dipoles,  $\mu^{\text{ind}}$ , were obtained by integrating the electronic density for  $\infty < z < -1.8$  Å (gray area) c) Dependence of  $|\mu^{\text{ind}}|$  at 532 nm with respect to the kick strength at different tip-molecule relative positions.

To analyze the shape of the local electromagnetic field,  $\partial\tilde{\Phi}_{\text{tip}}/\partial z$ , we fitted it by a Gaussian function defined as

$$f(x, y) = A_0 e^{-(a((x-x_0)^2) + 2b(x-x_0)(y-y_0) + c((y-y_0)^2))} + B_0, \quad (25)$$

with  $a = (\cos(\theta)^2)/(2\sigma_x^2) + (\sin(\theta)^2)/(2\sigma_y^2)$ ,  $b = -(\sin(2\theta))/(4\sigma_x^2) + (\sin(2\theta))/(4\sigma_y^2)$ ,  $c = (\sin(\theta)^2)/(2\sigma_x^2) + (\cos(\theta)^2)/(2\sigma_y^2)$ , and  $A_0$  and  $B_0$  are a normalization constant and an offset, respectively.

Fig. S5 and S6 show two-dimensional Gaussian fits of  $\partial\tilde{\Phi}_{\text{tip}}/\partial z$  for tip-A model structure at 4 Å and 1.5 Å below the tip apex, respectively. On the former case, the Gaussian fit reproduces to some extent the reference TD-DFT data, but the fit presents a more moderate

increase at its center and underestimates the maximum intensity by 20%. On the latter case, a Gaussian fit completely misses the rapid variation and sign change of local field observed in the reference data. In Fig. S7 and S8, we show analogous plots for the tip-B model structure. While a Gaussian fit for the data at 1.5 Å is clearly inadequate, at 4.0 Å the fit looks acceptable besides the fact it cannot capture the radial asymmetry present in the reference data. We remark that in this work only tip-molecule distances greater than 4 Å have been considered.

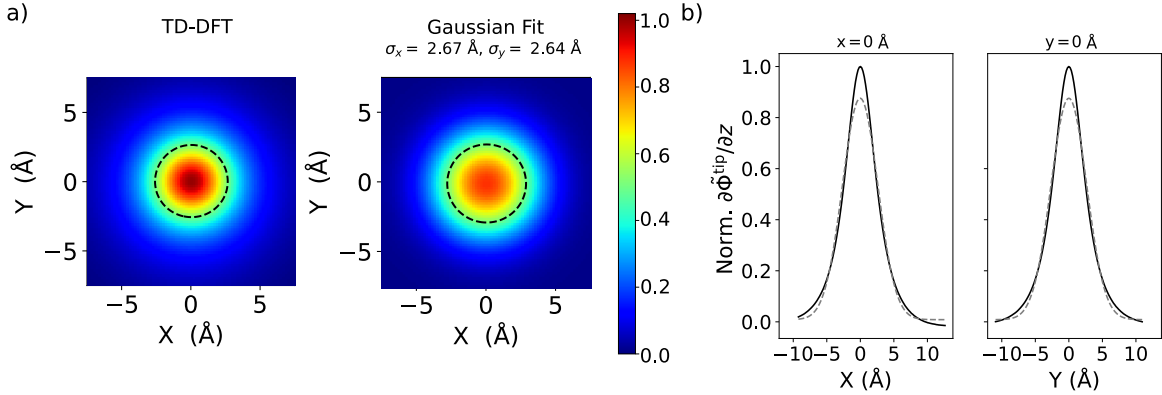


FIG. S5: Gaussian fit of a two-dimensional slice of  $\partial\tilde{\Phi}_{\text{tip}}/\partial z$  for tip-A model structure at 4 Å below the tip apex. a) Normalized two-dimensional heat map. Dashed lines represent 0.5 isocontours. b) One dimensional cuts along  $x=0$  Å and  $y=0$  Å. Solid black line and gray dashed line represent the reference and Gaussian fit data, respectively. The tip apex was set at the origin of coordinates as depicted in Figure 2a in the main text.

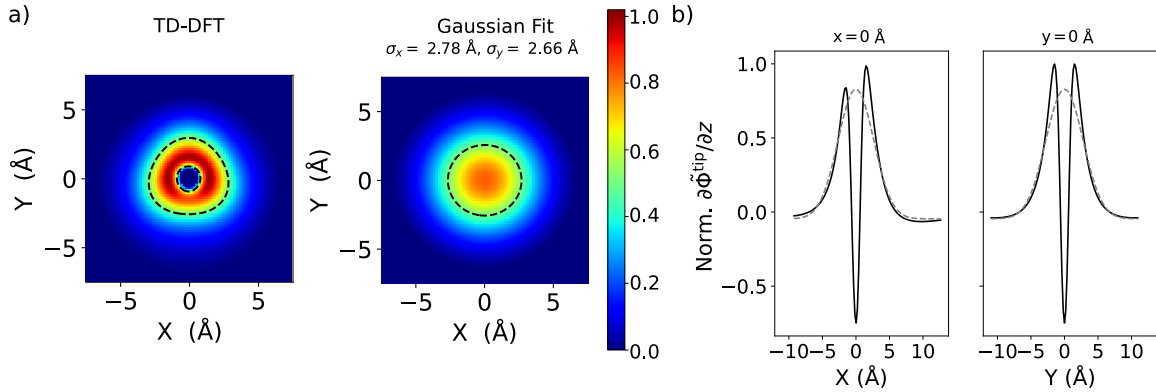


FIG. S6: Same as figure S5 for a slice taken at 1.5 Å below the tip apex.

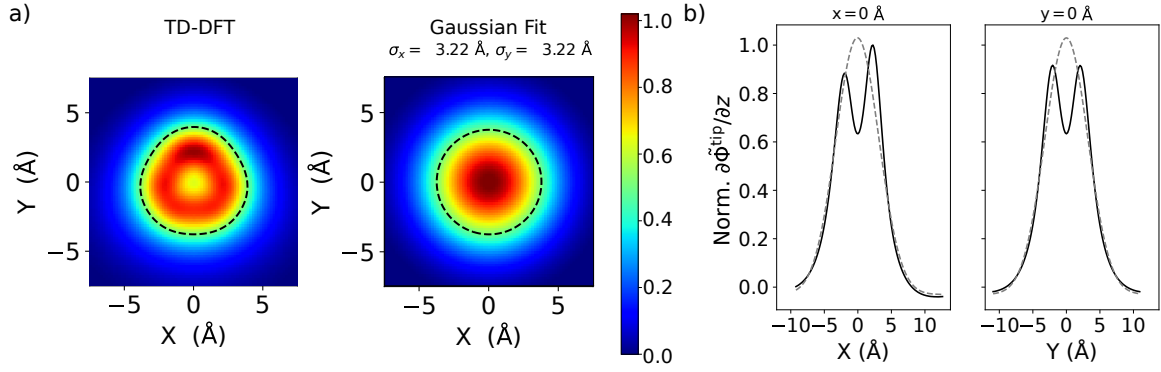


FIG. S7: Same as figure S5 for a tip-B model structure.

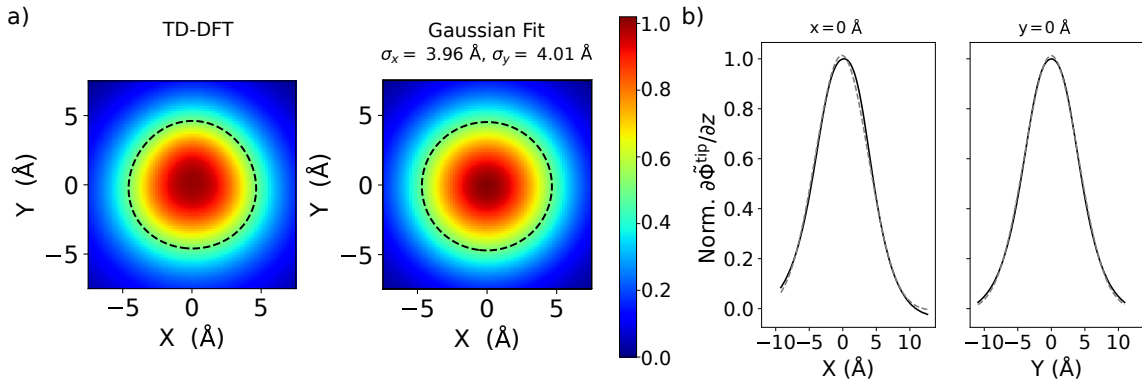


FIG. S8: Same as figure S6 for a tip-B model structure.

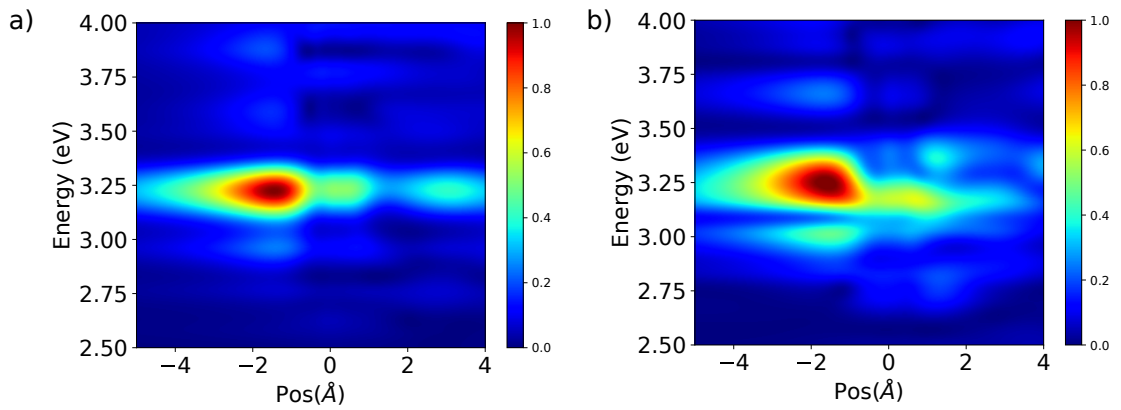


FIG. S9: Comparison of  $\tilde{\Phi}_{\text{tip}}$  of Tip-A computed using a) LDA and b) PBE exchange correlation functionals.

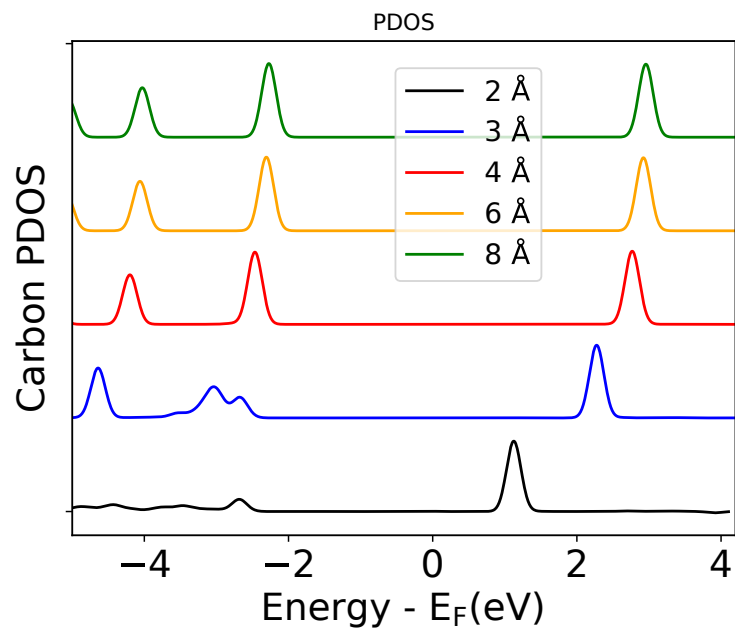


FIG. S10: Projected electronic density of states of benzene molecules as a function of molecule-tip distance.

#### IV. ADDITIONAL TERS IMAGES

In Fig. S11 and S12, we show further TERS images for the benzene and TCNE molecules, respectively.

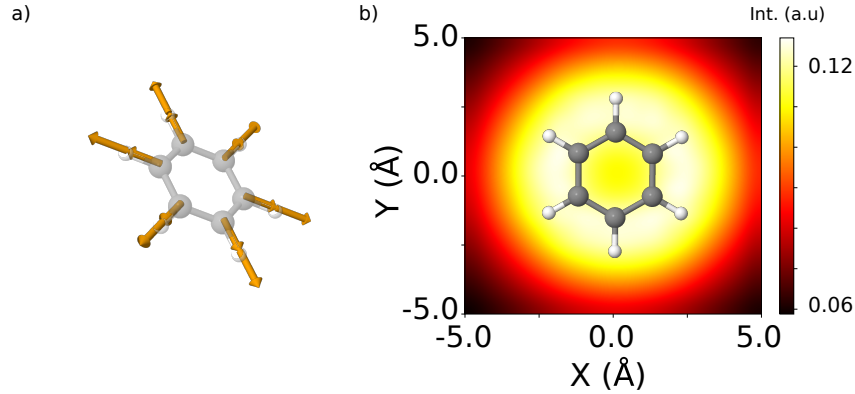


FIG. S11: TERS simulation of gas-phase benzene from local-field DFPT calculations. Normal mode displacements (a) and TERS images (b) of the the  $1015 \text{ cm}^{-1}$  ( $a_{1g}$ ) mode for a molecule-tip apex distance of  $4 \text{ \AA}$ .

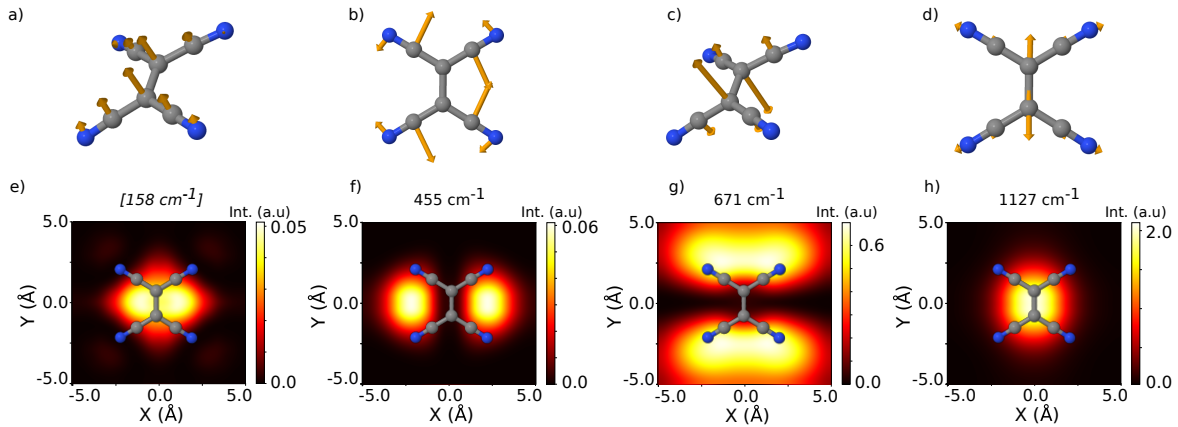


FIG. S12: Simulated TERS images of TCNE in isolation, but at the adsorbed geometry with the addition 1 electron to the molecule with out further geometry relaxation (TCNEads-1e). a), b), c) and d) Normal mode displacements of selected vibrational modes of TCNE@Ag(110). The surface has been deleted for clarity. e), f), g) and h) TERS images of the depicted normal modes for TCNEads. In all cases a molecule-apex distance of  $4 \text{ \AA}$  was employed. Frequency within square brackets in panel e) denotes the lack of an equivalent normal mode eigenvector in the TCNEads1e calculation.

## REFERENCES

- <sup>1</sup>V. Blum, R. Gehrke, F. Hanke, P. Havu, V. Havu, X. Ren, K. Reuter, and M. Scheffler, *Comp. Phys. Comm.* **180**, 2175 (2009).
- <sup>2</sup>J. P. Perdew and Y. Wang, *Phys. Rev. B* **45**, 13244 (1992).
- <sup>3</sup>A. H. Larsen, J. J. Mortensen, J. Blomqvist, I. E. Castelli, R. Christensen, M. Dulak, J. Friis, M. N. Groves, B. Hammer, C. Hargus, E. D. Hermes, P. C. Jennings, P. B. Jensen, J. Kermode, J. R. Kitchin, E. L. Kolsbjerg, J. Kubal, K. Kaasbjerg, S. Lysgaard, J. B. Maronsson, T. Maxson, T. Olsen, L. Pastewka, A. Peterson, C. Rostgaard, J. Schiøtz, O. Schütt, M. Strange, K. S. Thygesen, T. Vegge, L. Vilhelmsen, M. Walter, Z. Zeng, and K. W. Jacobsen, *J. Phys.: Condens. Matter* **29**, 273002 (2017).
- <sup>4</sup>X. Andrade, D. Strubbe, U. De Giovannini, A. H. Larsen, M. J. T. Oliveira, J. Alberdi-Rodriguez, A. Varas, I. Theophilou, N. Helbig, M. J. Verstraete, L. Stella, F. Nogueira, A. Aspuru-Guzik, A. Castro, M. A. L. Marques, and A. Rubio, *Phys. Chem. Chem. Phys.* **17**, 31371 (2015).
- <sup>5</sup>N. Tancogne-Dejean, M. J. T. Oliveira, X. Andrade, H. Appel, C. H. Borca, G. Le Breton, F. Buchholz, A. Castro, S. Corni, A. A. Correa, U. De Giovannini, A. Delgado, F. G. Eich, J. Flick, G. Gil, A. Gomez, N. Helbig, H. Hübener, R. Jestädt, J. Jornet-Somoza, A. H. Larsen, I. V. Lebedeva, M. Lüders, M. A. L. Marques, S. T. Ohlmann, S. Pipolo, M. Rampp, C. A. Rozzi, D. A. Strubbe, S. A. Sato, C. Schäfer, I. Theophilou, A. Welden, and A. Rubio, *J. Chem. Phys.* **152**, 124119 (2020).
- <sup>6</sup>O. A. Douglas-Gallardo, M. Berdakin, T. Frauenheim, and C. G. Sánchez, *Nanoscale* **11**, 8604 (2019).